Renewable Energy 99 (2016) 800–812

Contents lists available at ScienceDirect

Renewable Energy

journal homepage: www.elsevier.com/locate/renene

Dynamic response and viscous effect analysis of a TLP-type floating wind turbine using a coupled aero-hydro-mooring dynamic code

Macheng Shen [a], Zhiqiang Hu [a, b, *], Geliang Liu [a]

[a] State Key Laboratory of Ocean Engineering, Shanghai Jiao Tong University, China
[b] School of Marine Science and Technology, Newcastle University, Newcastle upon Tyne, NE1 7RU, United Kingdom

ARTICLE INFO

Article history:
Received 31 May 2015
Received in revised form
13 March 2016
Accepted 21 July 2016

Keywords:
Floating wind turbine
TLP
Dynamic response
Viscous drag force
Pitch resonance

ABSTRACT

This paper presents a coupled dynamic motion response analysis of a floating wind turbine using an in-house code, CRAFT (Coupled Response Analysis of Floating wind Turbine). Viscous drag forces on horizontal pontoons are carefully calculated, and a nonlinear spectral method is applied to efficiently solve the coupled tendon dynamics. Viscous drag forces and tendon dynamics are two important factors when assessing a tension-leg platform (TLP)-type floating wind turbine in a time-domain simulator. The analysis object is the NREL 5 MW Wind Turbine, which is supported by a three-leg mini-TLP platform. Simulations of the free decay and response amplitude operator (RAO) tests are conducted using CRAFT as well as FAST, another commonly used code. The obtained results are compared with experimental results to verify the capability of CRAFT. Viscous drag force induces higher harmonic pitch resonance, which is most prominent when the wave period is three times the natural period of the pitch and the wave height reaches a threshold. Springing motion is identified and found to be caused by this resonant pitch motion. Time-domain statistics show that extreme increases in tendon loads caused by springing as well as pitch and tendon tension probability distributions are non-Gaussian in random sea states. In addition, the resonant pitch motion is significantly reduced by aerodynamic damping.

1. Introduction

Offshore wind energy is a promising renewable energy source, and deep water zones provide steady and strong winds, which promise stable, high-quality electrical energy production. An offshore wind turbine supported by a floating platform is one of the most cost-efficient choices for harvesting energy from high-wind areas with water depths exceeding 50 m. However, because these wind turbines are supported by a floating body, the response of the system is simultaneously dominated by several coupled loads, including the aerodynamic load, hydrodynamic load and mooring line load. These coupled dynamic responses of a floating wind turbine to wind and wave loads are complicated and must be solved in a time domain to capture transient and nonlinear effects.

Among the compliant floating platforms widely used in the offshore oil industry, tension-leg platforms (TLPs) provide steady motion because of the high stiffness of their tendon mooring system, which generates wind power of good quality [1]. Independent 5 MW TLP-type wind turbine designs include designs by Concept Marine Associates (CMA) [2], Massachusetts Institute of Technology and Italian Enel group (MIT/Enel) [3], MIT and National Renewable Energy Laboratory (MIT/NREL) [4], and University of Maine [5]. These designs represent a variety of displacements from 846 tons to 12,187 tons, with stiffness provided by 3–8 tendons, and diameters at the water line ranging from 4.5 m to 18 m. With these drastically different mass and geometric properties, the dynamic response of each wind turbine system is unique and must be analyzed using suitable methods. Furthermore, because of their high stiffness, TLPs are susceptible to high-frequency excitations that can produce resonant heave and pitch motions and cause fatigue damage to the tendons. Thus, these high-frequency excitations should be observed in a time-domain simulator, and a coupled dynamic analysis should be performed to verify its feasibility. There are several possible sources of high-frequency excitations: aerodynamic loads caused by turbulent wind imposed on the rotor and tower; second-order wave forces imposed on the platform; vortex-shedding-induced lifting forces imposed on the tendons; and

* Corresponding author. School of Marine Science and Technology, Newcastle University, Newcastle upon Tyne, NE1 7RU, United Kingdom.
E-mail address: zhqhu@sjtu.edu.cn (Z. Hu).

http://dx.doi.org/10.1016/j.renene.2016.07.058
0960-1481/

viscous drag forces imposed on the surface piercing column and pontoons and tendons. Among these excitations, the hydrodynamic loads exceed the aerodynamic loads, thus dominating the system response. The viscous drag force is proportional to the square of the wave height and causes a mean displacement of surge and pitch motion that is proportional to the cube of the wave height [6]. Shen et al. [7] showed that viscous drag force can induce nonlinear higher harmonic vibrations in surge motion. Although the amplitudes of higher harmonic surge components are small, they can cause pitch resonance motion because of the inertial and hydrodynamic coupling between the surge and pitch if the frequencies of the higher harmonics are close to the natural frequency of the pitch. Furthermore, a strong interaction among the tower, platform and tendons has been observed in previous numerical simulations. Therefore, it is also necessary to analyze the coupled high-frequency response of floating wind turbines supported by TLPs because of the viscous drag force, especially in extreme sea conditions.

In Shen et al. [7], the viscosity-induced high-frequency dynamic responses in both regular and irregular waves were investigated. Regular waves were examined using an analytical method, which was difficult to achieve for irregular waves. Therefore, a numerical analysis using FAST was applied, although FAST may not provide quantitatively correct predictions of the resonant amplitude because it adopts a quasi-static mooring model, which neglects viscous drag forces on tendons and overestimates the pitch resonant amplitude to some extent because the coupling between the tendons' axial and transversal motions has a non-trivial contribution to the pitch damping. In addition, the experimental data presented in Steward et al. [8] indicated that the surge damping of a TLP floating wind turbine is nonlinear and amplitude dependent, which may be related to viscous drag, although this aspect is partially neglected in FAST. For high-frequency motion, potential damping caused by wave radiation is negligible, whereas aerodynamic damping and viscous damping are critical for determining the pitch resonant amplitude. FAST v7 is a globally used code for solving aerodynamic, hydrodynamic and control problems related to floating wind turbines. Therefore, the simulation results with respect to the linear responses given by CRAFT is compared with those given by FAST v7 for verification purpose.

Additionally, tendon dynamics are also essential for determining the extreme dynamic response of TLPs. High-frequency resonant pitching is responsible for tendon springing and ringing phenomena, and the resulting high-frequency variations in the axial tension may cause the parametric vibrations and Mathieu instability [9]. Many scholars have studied the coupled dynamic motion of TLPs and their tendons. Paulling and Webster [10] discussed these aspects and concluded that the coupling effect is important. Ahmad [11] studied the coupled responses of TLPs by retaining the nonlinearities caused by the drag force, variable submergence, and large deformation and by randomly varying the tether tension, and he showed that the heave response and tendon tension are critically affected by the coupling between degrees of freedom. Gadagi and Benaroya [12] studied the nonlinear dynamic response of an axially loaded tendon via the finite difference method (FDM). At low tension, the axial motion is mainly induced by geometry; thus, the geometric nonlinearity caused by lateral motion is important. Roald et al. [13] calculated the quadratic transfer function for the second-order wave forces on a mini-TLP and determined that these forces are an important source of high-frequency excitation and likely contribute to tendon tension variations. Chen et al. [14] applied a coupled dynamic analysis code accurate to the second order to analyze the response of a mini-TLP and solved the tendon dynamics using the FDM. These authors compared the results predicted by a coupled analysis and those predicted by an uncoupled analysis, which applied a quasi-static mooring model with experimental results, and they showed that the results of the coupled analysis were consistent with those of the experimental findings, whereas the uncoupled analysis failed to provide satisfactory predictions in the low- and high-frequency regimes.

In this work, an in-house coupled dynamic analysis program (CRAFT) for TLP-type floating wind turbines is presented. This model accounts for the nonlinear tendon dynamics and viscous drag force imposed on the horizontal pontoons. Free decay tests and response amplitude operators (RAOs) are calculated and compared with the results provided by FAST and model test results from Koo et al. [5] and Stewart et al. [8] to validate the CRAFT simulation results. The effects of viscous drag force, aerodynamic force, and mooring models on the dynamic response of the surge, pitch and tendon tensions in regular waves, random sea states and joint wind-wave sea states are investigated using a frequency domain spectrum analysis and time-domain statistical analysis. Emphasis is placed on the coupled pitch resonance induced by the viscous drag force and resulting springing and extreme loads.

2. Theory and method

2.1. Aerodynamic load

In this work, only steady-state winds are considered, and the corresponding aerodynamic force results in a mean surge displacement and is balanced by the horizontal component of the tendon tension. A pitch moment is also induced, which causes an increase in the tension on the windward side and decrease on the leeward side. In addition, the aerodynamic force presents significant damping of the pitch motion, which is crucial for reducing high-frequency pitch resonant motion. Nevertheless, under extreme sea conditions, the turbine is parked and blades are feathered (90° pitch angle) to avoid large aerodynamic forces that could substantially damage the blades. In such situations, aerodynamic damping is small compared with that of the operating conditions.

Aerodynamic forces are calculated using the blade element momentum (BEM) theory, which is a combination of blade element theory and momentum theory. Although efficient, BEM theory neglects radial aerodynamic interactions by assuming two-dimensional flow at each radius; moreover, the derivation of momentum theory is based on quasi-static flow. Nevertheless, BEM theory is sufficiently accurate for predicting mean wind forces when the incoming flow does not vary rapidly with time.

A tip loss model, hub loss model and Glauert correction are also adopted to fix the induction factor because of a finite blade number, vortexes shed by the hub and turbulent wake, respectively. The effect of dynamic stall is not taken into consideration in this work. Further details regarding the theory and implementation of the BEM theory can be found in Moriarty and Hansen [15] and/or Burton [16].

The dynamic effect of aerodynamic loads induces additional coupling between the surge and pitch motions of the platform. For fixed rotor speeds and blade pitch angles, the local angle of attack is almost linearly related to the relative incoming flow velocity, whereas the magnitude of total relative velocity is approximately unchanged because the dominant component is the tangential velocity, which is determined by the rotor angular velocity. Consequently, the lifting force on each blade element is almost linearly related to the relative incoming flow velocity, which is similar to the total thrust force as an integration of blade element forces. As a result,

$$F_T = F_{steady} + C_T V_{disturb}, \tag{1}$$

where F_T denotes the rotor thrust force, F_{steady} denotes the rotor thrust force caused by steady-state winds without platform motion disturbance, $C_T = \frac{\partial F_T(V)}{\partial V}\Big|_{V_{steady}}$, and $V_{disturb}$ is the deviation of the relative velocity from the steady-state velocity caused by surge and pitch motion.

Assuming the mean wind direction is oriented in the positive x direction, it follows that

$$V_{distrub} = -\dot{x}_1 - \dot{x}_5 l, \tag{2}$$

where x_1 denotes the surge displacement, x_5 denotes the pitch displacement, and l denotes the distance between the rotor center and a reference point that is assumed to be on the static water plane.

Substituting (2) into (1) provides the following:

$$F_T = F_{steady} - C_T\dot{x}_1 - C_T\dot{x}_5. \tag{3}$$

Thus, the induced pitch moment is equal to

$$M = F_T l = F_{steady} l - C_T\dot{x}_1 l - C_T\dot{x}_5 l^2. \tag{4}$$

Eqs. (3) and (4) show that the presence of aerodynamic forces introduces an additional coupling between surge and pitch. On the right-hand side of (3), the first term results in a mean surge displacement, the second term is the source of aerodynamic damping for surge, and the third term represents the surge excitation caused by pitch. Similarly, on the right-hand side of (4), the second term represents the pitch excitation caused by surge and the third term is the aerodynamic damping of pitch. This derivation shows consistency with the experimental findings about aerodynamic damping presented in Koo et al. [5].

2.2. Hydrodynamic loads

Hydrodynamic loads are calculated using a hybrid potential-Morison equation approach, wherein the inertial and radiation forces are predicted using potential theory, and the viscous force is approximated by the Morison equation. For large-volume structures, the potential flow and rigid body assumptions simplify the problem while maintaining the accuracy of the predicted hydrodynamic loads. For smaller structural components, viscosity is important because of flow separation, which results in a drag force that is proportional to the square of the velocity.

By assuming that the wave amplitude and body motion are small, the potential flow problem can be split into first-order, second-order and higher-order problems with respect to the wave height. According to first-order potential theory, the governing equations of platform motion can be written as follows [17]:

$$\sum_{\beta=1}^{6}\left[M_{\alpha\beta} + \mu_{\alpha\beta}(\infty)\right]\ddot{X}_\beta + \int_{-\infty}^{t} L_{\alpha\beta}(t-\tau)\ddot{X}_\beta(\tau)d\tau + C_{\alpha\beta}X_\beta = F_\alpha^D + F_\alpha^{FK} + F_\alpha^M + F_\alpha^V, \tag{5}$$

where $M_{\alpha\beta}$ represents the inertia matrix; $\mu_{\alpha\beta}$ represents the added mass matrix of infinite frequency; $L_{\alpha\beta}$ represents the matrix kernel of convolution, which reflects memory effects of the free surface; $C_{\alpha\beta}$ represents the hydrostatic restoring matrix; F_α^D represents the diffraction forces; F_α^{FK} represents the Froude-Kriloff (F-K) forces; F_α^M represents the mooring forces; and F_α^V represents the viscous drag forces imposed on the columns and pontoons.

The added mass, radiation damping, diffraction and F-K forces can be determined from a frequency domain code such as WAMIT [18]. Subsequently, an integral transformation is used to calculate the convolution kernel. Mooring forces are determined from the tendon dynamic equations. Viscous and inertial forces on the structural components per length are calculated via the Morison equation:

$$dF = \frac{1}{2}\rho D C_D|U-u|(U-u) + \frac{1}{4}C_M\rho\pi D^2\frac{\partial U}{\partial t} - \frac{1}{4}(C_M-1)\rho\pi D^2\frac{\partial U}{\partial t}, \tag{6}$$

where U denotes the ambient wave velocity and u denotes the velocity of the structural component induced by platform motion. Only the viscous term is calculated and imposed on the column and pontoons because the inertial terms are included in the added mass, F-K forces, diffraction forces and radiation forces. Both the viscous and inertial terms are calculated as hydrodynamic forces on the tendons.

The added mass and drag coefficient of the tendons are $C_M = 2.0$ and $C_D = 1.0$, respectively [6,19]. The drag coefficient of the surface piercing column is 0.7, and the drag forces on the three rectangular sectional pontoons are also calculated, which is not performed in FAST. The drag coefficients of sharp-edged bodies were investigated by Bearman et al. [20], and their experimental results showed that the drag coefficient is approximately 3.0 for a facing square and 5.0 for a diagonal square. Because the pontoon cross-sections are rectangular, the average of the length and width is chosen as the equivalent diameter. The relative velocity between a fluid particle and structure is decomposed into a component perpendicular to the cross-section and a component parallel to the cross-section, although only the latter contributes to the drag force.

2.3. Tendon dynamics

Determining expressions for the positioning and dynamic capabilities of the tendons of TLP-type wind turbines is challenging. The vertical and horizontal displacements of the tendons are expanded as a superposition of a set of trigonometric basis functions, and a set of nonlinearly coupled ordinary differential equations governing the expansion coefficients is derived from the Lagrange equation. This method for solving partial differential equations is commonly known as the spectral method (SM). The SM usually has higher accuracy and resolution than the FDM or FEM approaches for smooth solutions and assumes the same calculation time. The formulation is presented as follows

$$u(x,t) = \frac{u_0(t)x}{l} + \sum_{n=1}^{N_1} a_n(t)\sin\left(\frac{n\pi x}{l}\right), \tag{7}$$

$$v(x,t) = \frac{v_0(t)x}{l} + \sum_{n=1}^{N_2} b_n(t)\sin\left(\frac{n\pi x}{l}\right), \tag{8}$$

$$w(x,t) = \frac{w_0(t)x}{l} + \sum_{n=1}^{N_3} c_n(t)\sin\left(\frac{n\pi x}{l}\right), \tag{9}$$

where x represents the axial coordinate, with $x = 0$ representing the bottom end point connected to the anchor and $x = l$ representing the top end point connected to the fairlead; l represents the length of the tendon; u, v and$w$ represent the horizontal and vertical displacements, respectively; u_0, v_0 and w_0 represent the displacements of the top end point, which are determined by the platform motion; and a_n, b_n and c_n are the expansion coefficients.

The total kinematic energy can be written as follows

$$T = \frac{1}{2}\rho \int_0^l (\dot{u}^2 + \dot{v}^2 + \dot{w}^2)dx$$
$$= \frac{1}{2}\rho\left[\frac{\dot{u}_0^2 l}{3} + \frac{\dot{v}_0^2 l}{3} + \frac{\dot{w}_0^2 l}{3} + \sum_{n=1}^{N_1}\frac{\dot{a}_n^2 l}{2} + \sum_{n=1}^{N_2}\frac{\dot{b}_n^2 l}{2} + \sum_{n=1}^{N_3}\frac{\dot{c}_n^2 l}{2} + \sum_{n=1}^{N_1}\frac{(-)^{n+1}\dot{u}_0\dot{a}_n l}{n\pi} + \sum_{n=1}^{N_2}\frac{(-)^{n+1}\dot{v}_0\dot{b}_n l}{n\pi} + \sum_{n=1}^{N_3}\frac{(-)^{n+1}\dot{w}_0\dot{c}_n l}{n\pi}\right], \tag{10}$$

where ρ represents the linear density of the tendon, and the dots denote time derivatives.

The elastic potential energy caused by bending is much smaller than that caused by elongation unless the axial tension decreases to zero. Thus, bending energy is neglected, and the total elastic potential energy is approximated as follows:

$$U = \frac{1}{2}EA\int_0^l \varepsilon^2 dx, \tag{11}$$

$$\varepsilon = \sqrt{1 + 2w_x + u_x^2 + v_x^2 + w_x^2} - 1, \tag{12}$$

where E is Young's modulus, A is the section area, and ε is the axial strain.

Because $l \gg u \approx v \gg w$, which is caused by the tendon's high stiffness, it follows that $1 \gg u_x \approx v_x \gg w_x$, which implies that the nonlinear terms u_x^2 and v_x^2should be preserved during linearization to retain the major contribution of the geometric nonlinearity. As a result, the strain can be approximated to the leading order as follows:

$$\varepsilon = w_x + \frac{1}{2}u_x^2 + \frac{1}{2}v_x^2, \tag{13}$$

The elastic potential energy can be approximated as follows:

$$U = \frac{1}{2}EA\int_0^l \left(w_x + \frac{1}{2}u_x^2 + \frac{1}{2}v_x^2\right)^2 dx$$
$$= \frac{1}{2}EA\left[\frac{w_0^2}{l} + \sum_{n=1}^{N_3}\frac{(\pi n c_n)^2}{2l} + \int_0^l \left(w_x u_x^2 + w_x v_x^2 + \frac{1}{4}u_x^4 + \frac{1}{4}v_x^4 + \frac{1}{2}u_x^2 v_x^2\right)dx\right]. \tag{14}$$

The potential energy caused by gravity and buoyancy can be easily written and substituted into the Lagrange equation:

$$\frac{d}{dt}\left(\frac{\partial L}{\partial \dot{q}_k}\right) - \frac{\partial L}{q_k} = Q_k, \tag{15}$$

where $L = T - V$ is the Lagrangian; V is the total potential energy; q_k is the generalized coordinate, which is composed of the set of expansion coefficients a_n, b_n and c_n in this study; and $Q_k = \frac{\partial(\delta W)}{\partial(\delta q_k)}$ is the generalized force corresponding to q_k. In addition, the imaginary work δW corresponding to the imaginary displacement δq_k is calculated by applying the Morison equation to the hydrodynamic force imposed on the tendon.

Combining equations (10), (14) and (15) and considering the effects of gravity and buoyancy, the governing equations accurate to the first order are as follows:

$$\left(\frac{\rho l}{2} + \frac{(C_M - 1)\rho_w \pi D^2 l}{8}\right)\frac{d^2 a_n}{dt^2} = \frac{(-)^n l}{2\pi n}\left(\rho + \frac{(C_M - 1)\rho_w \pi D^2}{2}\right)\frac{d^2 u_0}{dt^2} - \frac{\partial W}{\partial a_n} + \frac{C_M \rho_w \pi D^2}{4}\int_0^l \frac{dU_x}{dt}\sin\frac{n\pi x}{l}dx + \frac{C_D \rho_w D}{2}\int_0^l \left(U_x - \frac{\partial u}{\partial t}\right)\left|U_x - \frac{\partial u}{\partial t}\right|\sin\left(\frac{n\pi x}{l}\right)dx, \tag{16}$$

$$\left(\frac{\rho l}{2} + \frac{(C_M - 1)\rho_w \pi D^2 l}{8}\right)\frac{d^2 b_n}{dt^2} = \frac{(-)^n l}{2\pi n}\left(\rho + \frac{(C_M - 1)\rho_w \pi D^2}{2}\right)\frac{d^2 v_0}{dt^2} - \frac{\partial W}{\partial b_n} + \frac{C_M \rho_w \pi D^2}{4}\int_0^l \frac{dU_y}{dt}\sin\frac{n\pi x}{l}dx + \frac{C_D \rho_w D}{2}\int_0^l \left(U_y - \frac{\partial v}{\partial t}\right)\left|U_y - \frac{\partial v}{\partial t}\right|\sin\left(\frac{n\pi x}{l}\right)dx, \tag{17}$$

$$\frac{\rho l}{2}\frac{d^2 c_n}{dt^2} + \frac{EAn^2\pi^2}{2l}c_n = \frac{(-)^n \rho l}{2\pi n}\frac{d^2 w_0}{dt^2} - \frac{\partial W}{\partial c_n} + \left[(-)^{n+1} + 1\right]\frac{(\rho_w \pi D^2 - \rho)gl}{\pi n}, \tag{18}$$

where ρ_w is the density of sea water, D is the tendon outer diameter, C_M and C_D are the mass and drag force coefficients, respectively, in

the Morison equation, U_x and U_y are the horizontal components of the wave velocity, and g is the gravitational acceleration. $W = \frac{1}{2}EA\int_0^l \left(w_x u_x^2 + w_x v_x^2 + \frac{1}{4}u_x^4 + \frac{1}{4}v_x^4 + \frac{1}{2}u_x^2 v_x^2 \right) dx$ is the nonlinear component of the elastic potential energy, whose partial derivatives should be evaluated numerically at each time step. The advantage of using the trigonometric expansion is that the fast Fourier transformation technique can be used to significantly reduce the calculation time. Structural damping was not considered in this work because it is assumed to be small compared with the hydrodynamic viscous damping.

Once the displacements of the top end point and their first and second time derivatives are determined, the right-hand sides of Eqs. (16)–(18) can be determined given a sea state. Subsequently, the equations can be integrated using a time marching scheme to the next time step.

Unlike the modal superposition method, which assumes small deflection and linearization, the spectral method can simulate the nonlinear interaction between axial and transversal motions to an arbitrary order. The geometric nonlinearity of large deflection and potential for instability are intrinsically included.

2.4. Procedure of the coupled numerical simulation

For simplicity, structural flexibility is not included in the model, and the entire wind turbine and platform are modeled as a rigid body. These assumptions result in a discrepancy in the natural frequency of pitch motion. To remedy this situation, pitch inertia is tuned to be larger than that calculated from the rigid body mass distribution so that the pitch natural frequency is equivalent to 0.32 Hz.

At each time step, the axial force at the top end point of each tendon is obtained by applying Eq. (13). The spectral expansion is truncated at $N = 4$ in this study, which means that a group of 12 coupled equations for each tendon are solved to determine the motion and tension. A convergence test is conducted to confirm that this number of equations is sufficient for obtaining good accuracy. The rigid body accelerations are then solved from Eq. (5), and the accelerations of the fairlead points are calculated assuming that the platform is a rigid body. Because the right-hand sides of Eqs. (16)–(18) are determined assuming a specified sea state and motion history, they are integrated to the next time step using the fourth-order Runge-Kutta method. The numerical stiffness of Eq. (18) was carefully treated because of the high axial stiffness of the tendons. The flow chart of the solver is shown in Fig. 1.

3. Description of the objective model

The floating wind turbine studied in this work is composed of the NREL 5 MW Wind Turbine (see Table 1) and TLP proposed by the University of Maine for use in the DeepCwind project [5] (see Table 2). During the simulation, the waves and winds are in alignment (see Fig. 2).

The total mass of the wind turbine is approximately equal to the mass of the TLP, which indicates that the dynamic coupling between the turbine and TLP should be strong. A significant shift in the pitch and roll frequencies from approximately 0.54 Hz with a rigid tower to 0.32 Hz with a flexible tower, which is caused by the coupling between tower bending and platform pitch motions, is observed and described in Roald et al. [13] (See Table 3). Compared with the platforms used in oil and gas industries, this TLP platform is much smaller, which implies that the viscous effect is relatively more important compared with that of typical offshore TLP platforms.

4. Verifications

In this section, the CRAFT code is verified through a comparative analysis with a TLP-type floating wind turbine, and published experimental data presented in Stewart et al. [8] are adopted for the verification. The experiment was implemented on a $1/50^{th}$ scale TLP type floating wind turbine model based on Froude scaling by the University of Maine. All the experimental results were extrapolated to the full scale. In the surge free decay test, the platform was displaced the full scale equivalent of 4 m in the surge direction and the surge displacement was recorded by an optical displacement sensor located near the tower base [8].

4.1. Comparison of period and damping coefficients using free decay cases

Damping is one of the most important factors affecting TLP-type wind turbines. Experimental results have shown that quadratic damping caused by viscous drag plays an important role in low-frequency zones where radiation damping vanishes [8]. Surge free decay is simulated by CRAFT and FAST and shown in Fig. 3. CRAFT# denotes the free decay result without including the viscous drag force effects on the pontoons, whereas FAST, approximates the tendon mooring system by quasi-static mooring lines, which neglects the inertial effect. To remedy this situation, the platform mass applied in FAST includes the mooring mass listed in Table 2. This is done by adding two third of the total dry mass onto the platform. Because of the high tendon tension, the shape of the tendon can be well approximated as a straight line, which indicates the horizontal velocity of each element of the tendon is proportional to its distance from the anchor. As a result, the equivalent inertia is one third of the tendon mass if there is no ambient fluid and it should be doubled accounting for the added mass effect in water if the majority of the ambient fluid is assumed to be ideal. The quadratic damping ratio caused by viscous drag force in both the simulations and experiments were calculated using the method proposed by Hoff [21] and are summarized in Table 4. The results show that the lack of viscous drag in the numerical simulation leads to a large underestimation of the surge free decay damping (see Fig. 3 and Table 4.

The free decay results obtained using CRAFT show an amplitude-dependent characteristic, which can be observed from the free decay curve. The amplitude-dependent damping is also indicated by the experimental results and may have been caused by the viscous drag force. Therefore, the CRAFT simulation results are relatively close to the free decay curve obtained by the experimental findings presented in Stewart et al. [8].

The natural period predicted by CRAFT is larger than that predicted by CRAFT#, which is caused by the damping effect of the viscous force on the pontoons. The natural period predicted by CRAFT# is larger than that predicted by FAST, which is believed to be caused by the damping effect of the viscous force on the tendons. The natural periods predicted by all three simulations are close to that of the experimental results.

The overall damping in CRAFT is slightly lower than that in the experimental decay results. This phenomenon has also been observed for the OC-3 Hywind Spar wind turbine, where the hydrodynamic damping of the real platform motion is not fully captured by summing the linear radiation damping and nonlinear viscous drag forces [22].

Nevertheless, the free decay results, especially the natural period and quadratic damping ratio, predicted by CRAFT are consistent with the experimental findings, which confirms that the viscous drag forces on the pontoons are critical to TLP wind turbines and should not be neglected in numerical simulations.

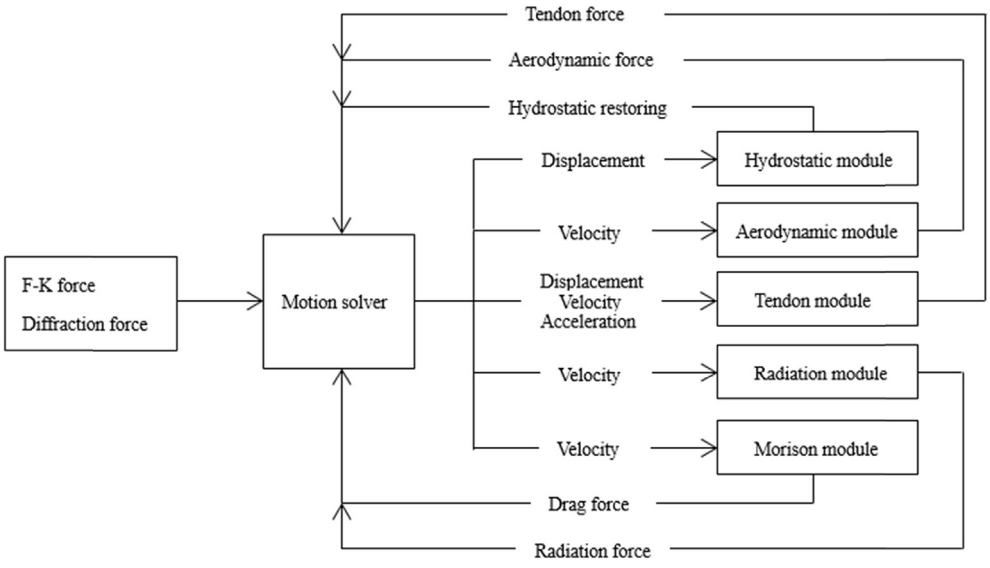

Fig. 1. Illustration of the procedure implemented in the coupled numerical simulation.

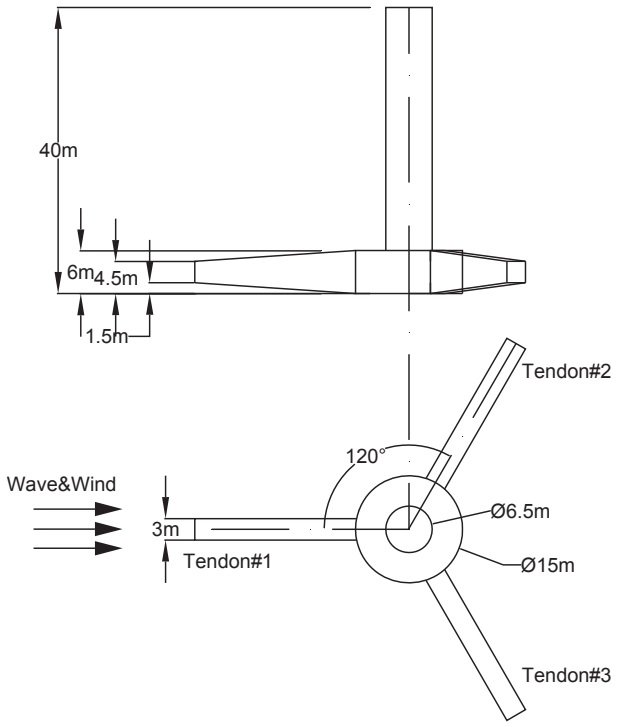

Fig. 2. Principal dimensions of the TLP [5].

4.2. RAO comparisons

Among all of six rigid-body modes of platform motion, surge and pitch are the two most important motions because they dominate the dynamic responses of the system. Thus, the capability of CRAFT to capture the response characteristics of these two motions is verified in this section. Surge RAOs are calculated from the CRAFT results for the white noise sea case and FAST results using a series of regular wave tests. The experiment results are obtained from the published results presented in Koo et al. [5]. The experiment was implemented on a 1/50th scale TLP type floating wind turbine model based on Froude scaling at Maritime Research Institute Netherlands. The six degree of freedom motions were measured by the optical tracking system [5]. The numerical and experimental results are shown in Fig. 4.

As shown in Fig. 4, the wave frequency surge RAOs calculated from these two approaches are comparable and consistent with the experimental results. The effect of viscous force appears to be insignificant in this case, which is mainly because the excitations and motions in the RAO cases are small. The magnitude of the viscous force is proportional to the square of the relative velocity; therefore, both exciting and damping effects of the viscous force are small, and the overall excitation and damping are dominated by first-order potential forces and radiation damping. Therefore, no significant difference is expected for surge RAOs where linear wave forces dominate. This consistency among surge RAOs suggests that both CRAFT and FAST can accurately predict the surge responses at typical wave frequencies.

Pitch motion is another important motion, and pitch RAOs are calculated for CRAFT and FAST. The results are shown in Fig. 5.

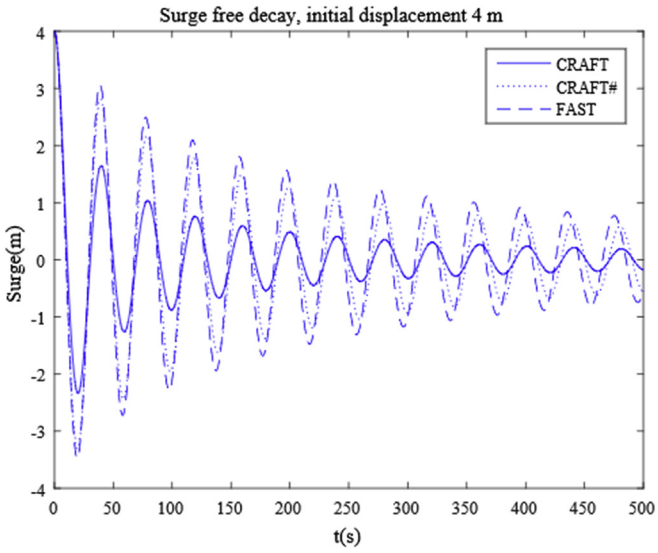

Fig. 3. Surge free decay test.

Table 1
Principal dimensions and mass properties of the NREL 5 MW wind turbine [5].

Item	Unit	Value
Power	MW	5.0
Tower Top Mass (Hub, Blades, and Nacelle)	kg	350,000
Rotor Diameter	m	126.0
Tower Mass	kg	249,718
Tower Height	m	77.6
Tower CG (% from Tower Base)	%	43.0

Table 2
Principal dimensions and mass properties[a] of the TLP [5].

Item	Unit	Value
Draft	m	30.0
Mass	kg	1361,000
Displacement	kg	2840,000
Anchor Radius	m	30.0
Water Depth	m	200.0
Tendon Diameter	m	0.6
Mass per Length (dry)	kg/m	289.8

[a] With wind turbine and moorings.

Table 3
Natural frequencies of the TLP with rigid and flexible wind turbine blades and tower [13].

Mode	Natural frequency (rigid) [Hz]	Natural frequency (flexible) [Hz]
Surge	0.0248	0.0248
Sway	0.0248	0.0248
Heave	0.9510	0.9467
Roll	0.5392	0.3191
Pitch	0.5399	0.3217
Yaw	0.0595	0.0595

The responses close to the pitch resonant frequency (0.32 Hz) predicted using CRAFT are much smaller than those predicted using FAST. The peak in the pitch RAOs predicted using CRAFT is approximately one-fifth of that predicted using FAST, and this difference may have been caused by the damping effect of the viscous drag force on the tendons. To verify this inference, the viscous force on the pontoons is removed, and the dynamic mooring lines are replaced by linear restoring forces in CRAFT. The corresponding results are shown with the dashed line and denoted as CRAFT* in Fig. 5. The peak value predicted using this method is close to that predicted using FAST, indicating that the discrepancy in the peak of the pitch RAOs is indeed caused by the damping effect. Because radiation damping vanishes at high frequencies, viscous damping on both the pontoons and tendons is important and dominates the resonant motions. The pitch natural frequency shifts from 0.319 Hz to 0.323 because of the removal of the viscous force and change in the tendon model. This difference is understandable because both the viscous damping effect and tendon inertial effect act to decrease the natural frequency.

Furthermore, the peak in the dashed line at low frequencies does not indicate a large pitch response to wave exciting forces at that frequency because this peak is caused by the inertial and hydrodynamic coupling with surge motion. Because white noise contains excitation over a large frequency zone that includes the surge resonant frequency, surge motion is resonated and exaggerated because of the lack of viscous damping, which results in a pitch response at such low frequencies. Therefore, this effect is caused by a faulty numerical model and further indicates the importance of including viscous damping in the numerical analysis.

In conclusion, both the free decay and RAO tests indicate that CRAFT is capable of providing quantitative results within a reasonable level of accuracy for the viscous induced pitch motion that is going to be discussed.

5. Discussion

In this section, pitch resonant motion induced by viscous drag force is investigated. Unlike the first-order potential forces, the viscous drag force is nonlinear and can cause higher harmonic surge responses. Because surge and pitch are highly coupled motions for floating wind turbines, pitch resonant motion can be excited if the frequency of one of the higher harmonic components coincides with the pitch natural frequency.

The effects of viscous drag force and tendon dynamics are studied by comparing the numerical simulation results obtained using three different approaches, which are summarized in Table 5. Approach 1 is the coupled dynamic analysis method applied in CRAFT; Approach 2 replaces the dynamic tendon model with linear restoring forces; and Approach 3 excludes the viscous drag forces on the columns and pontoons, although these forces on the tendons are preserved. The viscous force on tendons has been shown to be necessary not only for its important effects on damping and excitation but also for numerical stability.

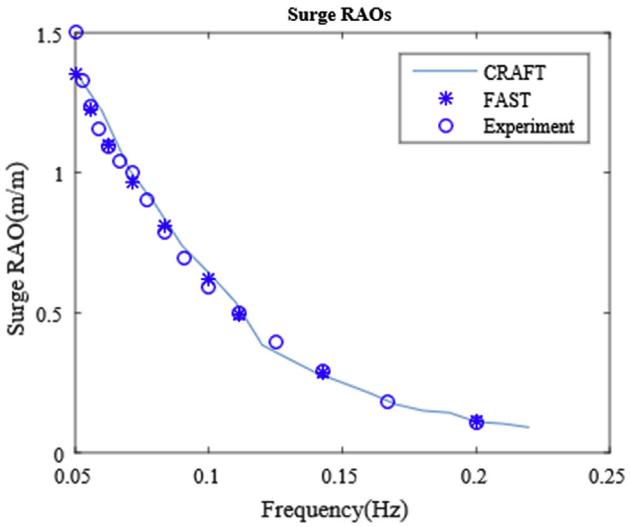

Fig. 4. Platform surge RAOs.

Table 4
Natural periods and damping ratios of surge motion.

	Average period	Quadratic damping	Percentage difference ratio in Qudratic damping
Unit	(s)	(1/m)	/
CRAFT	40.04	9.30E-03	9.7%
CRAFT#	39.88	5.70E-03	44%
FAST	39.45	4.40E-03	57%
Experiment	40.00	1.03E-02	/

5.1. Effects of higher harmonics

The magnitude and behavior of higher harmonic pitch responses differ, and these differences are investigated by analyzing the pitch responses in regular waves with specified periods. Regular wave tests with wave periods of 9.33 s, 15.55 s and 21.77 s are conducted, and their third, fifth and seventh harmonic excitations, respectively, excite pitch resonant motion. The wave parameters are listed in Table 6. An investigation of harmonics exceeding the seventh order requires wave periods longer than 28 s, which is seldom encountered within real sea states; thus, these orders are not discussed herein.

The pitch PSDs near the pitch resonant frequency are obtained after the transient motions because of initial conditions have decayed, and they are shown in Fig. 6.

In all three cases, pitch resonant motion is excited. In cases LC R1 and LC R2, the PSD predicted using Approach 1 is larger because the viscous effects on the columns, pontoons and tendons are included. The pitch PSDs predicted using Approach 2 are slightly smaller than those predicted using Approach 1, which indicates that the viscous forces on the columns and pontoons dominate the higher harmonic excitations because these forces are larger than those on the tendons because of their large cross-sectional areas. The viscous forces on the tendons have an increasing damping effect and decreasing excitation effect for increasing wave periods, which is indicated by the pitch PSDs predicted using Approach 3. In cases LC R2 and LC R3, the pitch PSDs are small, which means that the excitation effect of the tendon viscous force is much smaller than that in LC R1. In addition, in case LC R3, the pitch PSD predicted using Approach 2 is larger than the pitch PSD predicted using Approach 1, which indicates that the damping effect of the tendons overwhelms the excitation effects. Moreover, the magnitude of the higher harmonic pitch responses decrease for increases in the order. Therefore, higher (exceeding the seventh order) harmonic pitch responses are of less interest because of their small magnitudes.

5.2. Wave height effects

The dependence of higher harmonic responses on wave height is investigated using a series of regular wave cases with fixed periods and increasing wave heights. All of the simulations are conducted according to Approach 1. The peak value of the pitch PSD near the resonant frequency is determined based on the steady-state pitch time history shown in Fig. 7. The left side of Fig. 7 shows the pitch PSD excited by regular waves with a period of 9.33 s and wave heights ranging from 1 m to 12 m using an interval of 1 m. The right side shows that the PSD excited by regular waves with a period 15.55 s and wave heights ranging from 1 m to 14 m. Because the pitch resonant motion is induced by the nonlinear drag force, it is anticipated that the pitch resonant amplitude should grow nonlinearly with increasing wave height. The perturbation analysis applied in Shen et al. [7] indicates that the pitch resonant amplitude is proportional to a certain power of the wave height if the wave height is small. In Fig. 7, a cubic function is found to fit the first three data points that correspond to wave heights of 0 m, 1 m, and 2 m, and the fit has good accuracy. This finding indicates that the pitch resonant PSD is proportional to the wave height cubed or, equivalently, that the pitch resonant amplitude is proportional the wave height to the power of one and a half, if the wave height is small. Therefore, the pitch resonance induced by viscous drag grows more rapidly than the first-order motions and more slowly than the second-order motions for increasing wave heights.

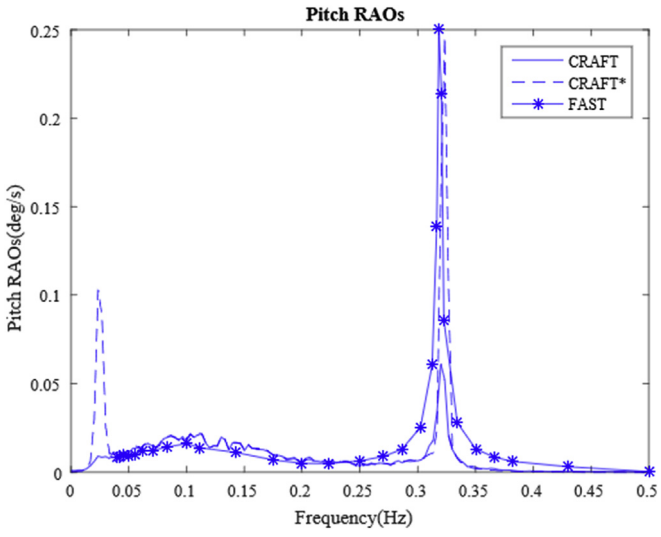

Fig. 5. Platform pitch RAOs.

In the case of the third harmonic pitch response corresponding to $T = 9.33$ s (Fig. 7, left), the simulated results exhibit deviation from the cubic function for wave heights exceeding 3 m. The PSD does not continue to increase with wave height and reaches a maximum at a wave height of approximately 9 m, decreasing with further increases in wave height. This result indicates that the strong nonlinear interaction between the pitch resonance and viscous drag force becomes complicated when wave heights are not small; thus, the relationship between pitch resonant motion and wave height cannot be simply described using polynomial functions. One of the reasons for the decrease in the pitch resonant PSD with increasing wave heights, which might appear contradictory at first, is the amplitude-dependent damping effect of the viscous force that can be observed by analyzing the quadratic drag term in the Morison equation. According to the Morison equation (6), viscous force is proportional to the square of the relative velocity:

$$dF_D \propto (U-u)|U-u|. \tag{19}$$

Pitch motion is small because of the high stiffness of the tendons; therefore, the induced structural velocity u is also small. Therefore, $u \ll U$ holds under moderate and severe sea state conditions, where U denotes the wave velocity. The viscous force can then be decomposed into one component that is independent of the structural velocity and another component that is proportional to the structural velocity:

$$dF_D \propto (U-u)|U-u| = |U|U - 2|U|u + O\left(u^2\right). \tag{20}$$

The second term on the right-hand side of Eq. (20) is always opposite that of the structural velocity and represents a damping force, whereas the damping coefficient $2|U|$ is proportional to the ambient wave velocity. Therefore, as the wave height increases, the damping effect of the viscous force also increases, implying that when the wave height is small, the pitch resonant PSD increases with wave height. When the wave height is sufficiently large, the viscous damping effect becomes important and prevents further increases in the pitch resonant PSD. In the case of fifth harmonic

Table 5
Simulation methods and settings.

Simulation approaches	Approach 1	Approach 2	Approach 3
Tendon model	Dynamic	Linear Restoring	Dynamic
Viscous force	Included	Included	Excluded

Table 6
Wave parameters for the regular wave cases.

	Wave period	Wave height	Higher-order harmonics
Case	(s)	(m)	/
LC R1	9.33	5.0	3rd
LC R2	15.55	5.0	5th
LC R3	21.77	5.0	7th

cannot be predicted based on responses to a series of regular waves; thus, such a response must be simulated independently. As indicated in Fig. 7, the most dangerous case in a real sea state is likely an irregular wave with a peak period of approximately 9.33 s and significant wave height of approximately 9 m.

Therefore, an irregular wave generated according to the Jonswap spectrum with $T_p = 9.4\ s$, $H_s = 8\ m$, and $\gamma = 2.2$ are simulated

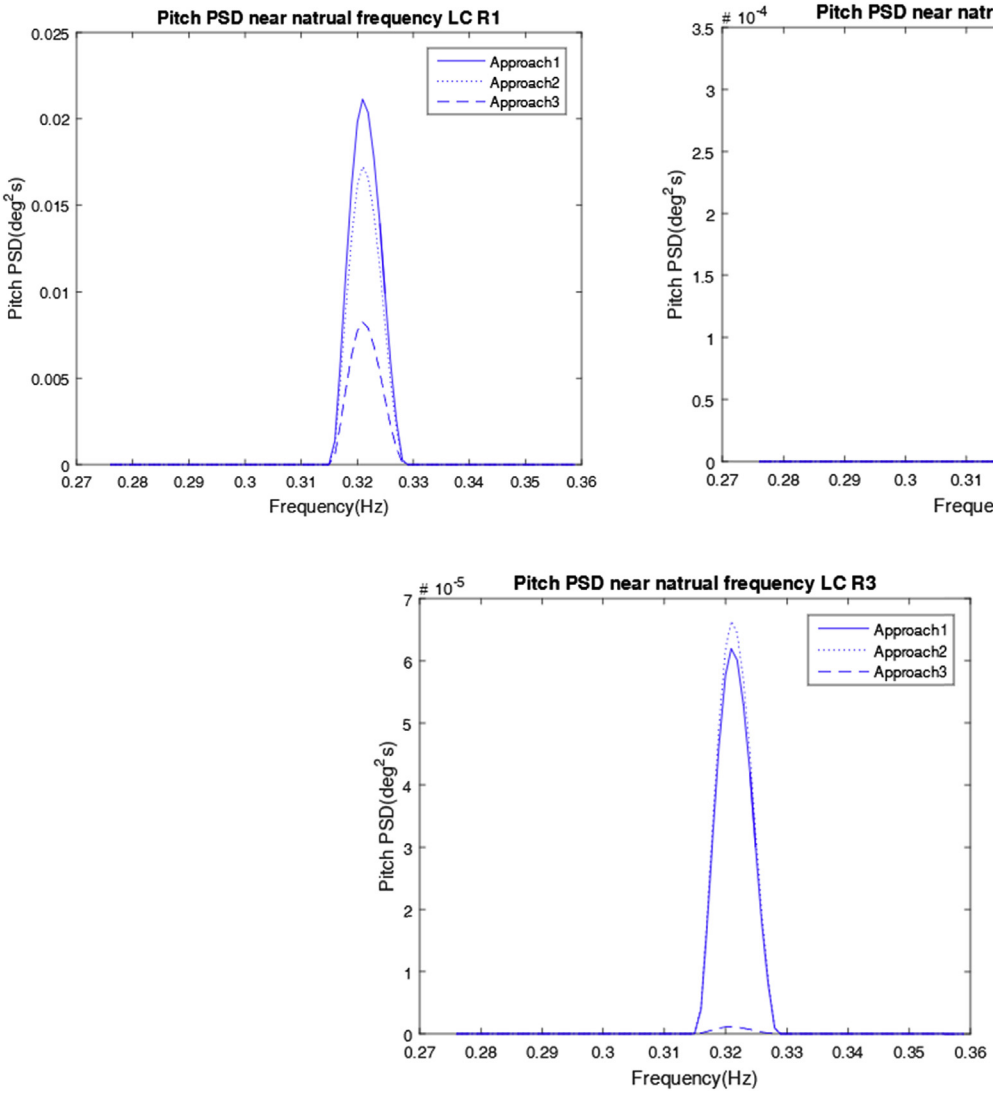

Fig. 6. Pitch PSDs near the natural frequency (0.32 Hz) for the regular wave cases.

pitch response corresponding to $T = 15.55$ s (right), the consistency between the pitch resonant PSD of large wave heights and cubic function is improved, whereas the effect of damping is still apparent, although it is not as pronounced because the pitch PSDs continue to increase with increasing wave heights. The amplitudes of the pitch PSDs in this case are much smaller than those excited by the third harmonic excitation.

5.3. Pitch resonance and corresponding loads in an extreme sea state

The pitch resonance induced by viscous drag is a highly nonlinear process; thus, the response in an irregular sea state using all three approaches. The wave spectrum is truncated at a frequency of 0.3 Hz, and wave components with frequencies higher than 0.3 Hz are intentionally excluded from the simulation so that the resonant pitch motion is purely induced by nonlinear viscous forces. The corresponding pitch PSDs are shown in Fig. 8.

According to Fig. 8, the pitch resonant motion induced by the third harmonic excitation is severe, and the peak in the pitch PSD at the resonant frequency is approximately three times that at the wave frequency. The total energy of the pitch resonant motion, which is characterized by the area under the pitch PSD curve, is the largest for Approach 1 and smallest for Approach 3. This finding is consistent with the results for the regular wave case and indicates that viscous forces acting on both the pontoons and tendons play an

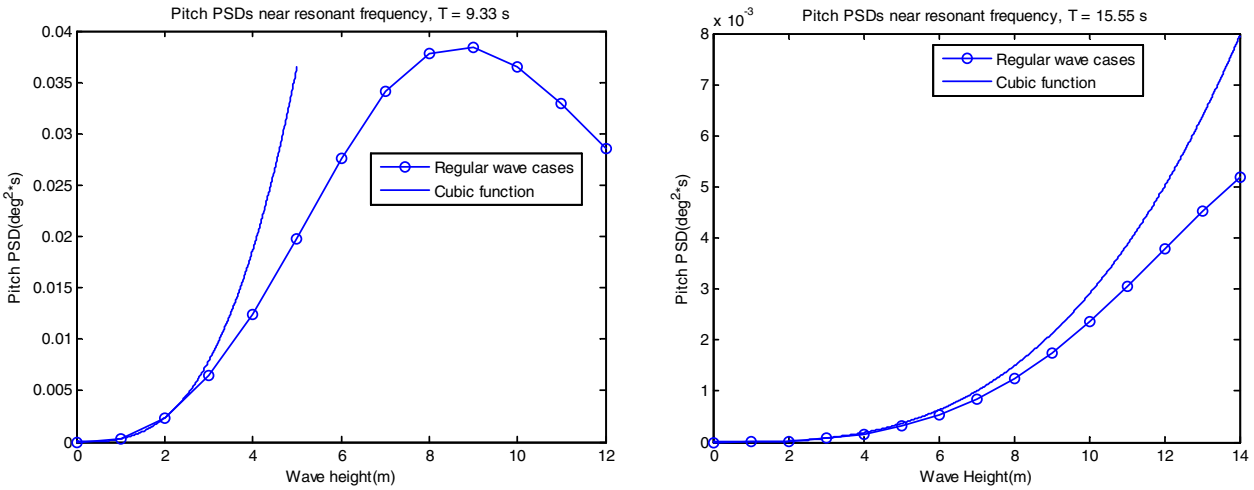

Fig. 7. Pitch PSDs near the resonant frequency under regular wave excitation with periods of 9.33 s and 15.55 s; cubic fits are also shown.

important role in resonant pitch motion.

The statistics for the surge, pitch, heave and tensions for tendons #1 and #2 are summarized in Table 7. Because tendons #2 and #3 are in symmetrical positions, the statistics for tendon #3 are not included in Table 7. The statistics include the skewness, which describes the degree of asymmetry of a distribution around its mean, and kurtosis, which describes the relative peakedness or flatness of a distribution relative to a Gaussian distribution [23].

The results show that the standard deviations of the pitch and tensions in tendons #1 and #2 predicted using Approach 1 and Approach 2 are larger than those predicted using Approach 3, which is caused by the excitation effect of the viscous force on the columns and pontoons, which is anticipated based on a comparison of the pitch PSDs in Fig. 8. The standard deviation of the tension in tendon #1 is approximately twice that of the tension in tendon #2, which is determined by the special position of tendon #1. The direction from fairlead point #1 to the rotation center of the platform, which is located at the center, is in alignment with the wave and wind directions, whereas those from fairlead points #2 and #3 have an angle of 60° relative to the direction of the waves and winds. Thus, when the platform pitches, the resulting tension variation in tendon #1 is doubled. Extreme loads are also important when considering the survivability of TLPs in severe sea states. One of the criteria for survivability is to avoid tendon slack. The minimum tension for tendon #1 predicted using Approach 2 decreases to less than one-fifth of its mean value, which is most likely a result of the exclusion of tendon damping. This finding represents one of the intrinsic limitations of linear mooring models. In addition, the set-down characteristic of a tension leg-type mooring system cannot be captured using linear mooring, which is illustrated in the incorrect heave motion skewness and kurtosis predicted using Approach 2. The kurtosis of the tension in tendon #2 is many times larger than its statistical standard error when the viscous forces on the columns and pontoons are simulated, which indicates that its probability distribution deviates substantially from a Gaussian distribution. The kurtosis of the pitch and tension in tendons #1 and #2 are all positive for Approaches 1 and 2 and negative for Approach 3. This result indicates that viscous forces increase the probability of extreme loads because a positive kurtosis indicates a fatter tail in the probability distribution function compared with that of a Gaussian distribution. The probability that the tension in tendon #2 will deviate from its mean value by three times its standard deviation is estimated by the ratio between the number of occurrences of this event and total number of samples based on the 2500 s simulation. The result is a ratio of 0.0078 for Approach 1 and 0.0021 for Approach 3, whereas a value of 0.0027 is expected for a Gaussian distribution. Therefore, viscous forces increase the occurrence of extreme loads because they can produce higher harmonic resonant pitch motions.

It is also worthy to note that there is little difference in the standard deviations of the tendon tension predicted by these three approaches, which means linear restoring models might be sufficient for the prediction of linear responses despite the presence of nonlinear responses. But when the tendon fatigue is of major concern, linear model seems to be insufficient, noted that in Fig. 8, Approach 2 underestimates the peak height near the resonance frequency by about 30% compared with Approach 1. This can induce the same amount of underestimation for the tendon tension if the tendon is modeled as linear. Although including tendon dynamic effect does not change the linear response a lot, it significantly increases the pitch resonant response. The reason for this discrepancy should be that natural frequencies of the tendon transversal modes are much higher than the linear wave frequencies but close to the pitch resonant frequency, so strong coupling between pitch resonant response and tendon dynamic response is expected.

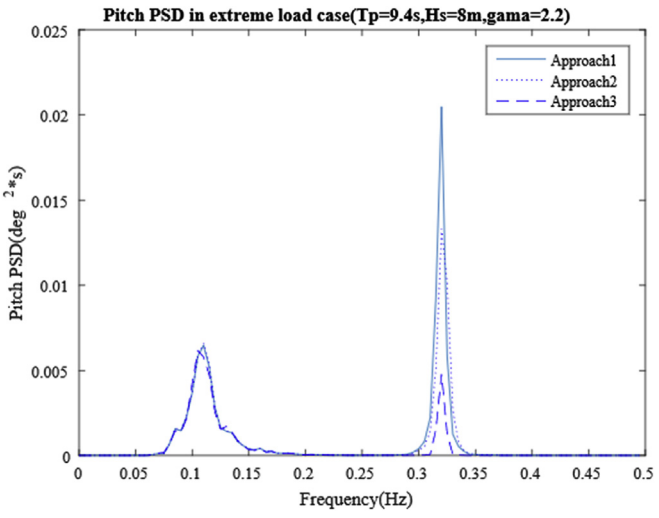

Fig. 8. Pitch PSDs for an extreme sea state with $Tp = 9.4$ s and $Hs = 8$ m.

Table 7
Statistics of motions and tendon tensions.

Approach 1	Surge (m)	Heave (m)	Pitch (deg)	Tension #1 (N)	Tension #2 (N)[a]
Mean	−4.174E-02	1.080E-01	−2.710E-04	4.992E+06	4.998E+06
Std.	9.853E-01	6.645E-03	4.417E-02	9.901E+05	5.771E+05
Skewness	−3.404E-02	−5.952E-01	4.361E-03	1.648E-02	1.276E-03
Kurtosis	−1.013E-01	1.407E+00	2.472E-01	1.768E-01	5.796E-01
Maximum	3.532E+00	1.289E-01	1.633E-01	8.732E+06	7.389E+06
Minimum	−3.092E+00	6.781E-02	−1.703E-01	1.300E+06	2.773E+06
Approach 2	Surge (m)	Heave (m)	Pitch (deg)	Tension #1 (N)	Tension #2 (N)
Mean	−4.775E-02	1.152E-01	−1.715E-04	4.990E+06	4.996E+06
Std.	1.012E+00	5.266E-03	4.276E-02	9.652E+05	5.646E+05
Skewness	−5.628E-02	8.840E-03	−3.471E-03	−3.253E-03	8.589E-03
Kurtosis	−9.696E-02	−9.104E-02	2.293E-01	1.789E-01	4.884E-01
Maximum	3.574E+00	1.341E-01	1.639E-01	8.757E+06	7.280E+06
Minimum	−3.151E+00	9.654E-02	−1.688E-01	9.599E+05	2.784E+06
Approach 3	Surge (m)	Heave (m)	Pitch (deg)	Tension #1 (N)	Tension #2 (N)
Mean	−2.704E-03	1.081E-01	−1.090E-04	4.995E+06	4.996E+06
Std.	9.548E-01	6.451E-03	3.834E-02	8.937E+05	4.848E+05
Skewness	2.106E-03	−5.993E-01	1.616E-02	1.777E-02	−3.118E-02
Kurtosis	−9.362E-02	1.427E+00	−1.440E-01	−4.452E-02	−7.156E-02
Maximum	3.143E+00	1.277E-01	1.321E-01	8.053E+06	6.709E+06
Minimum	−3.577E+00	6.524E-02	−1.435E-01	1.884E+06	3.353E+06

[a] Tension #1 and #2 refer to tensions in tendon #1 and #2, respectively.

5.4. Springing loads because of pitch resonance

Pitch resonance is likely to cause springing and ringing responses. The time history of the high-frequency component of the tension in tendon #1 is determined by applying a high-pass filter with a cutoff frequency of 0.24 Hz to the tension time history of tendon #1. The results are shown in Fig. 9.

Tendon springing occurs at the resonant frequency of pitch motion, and this strong springing load has significant impacts on tendon fatigue life. Nevertheless, standard criteria have not been decided upon to differentiate between springing and ringing [9]. Springing occurs when the extreme high-frequency tension does not exceed five to six times the standard deviation and the kurtosis of the high-frequency tension is less than or equal to 2.0 [24], whereas ringing occurs if the extreme high-frequency tension exceeds seven times the standard deviation and the kurtosis of the high-frequency tension is greater than 2.0 [25]. Table 8 shows the statistics for the high-frequency pitch and tensions in tendons #1 and #2.

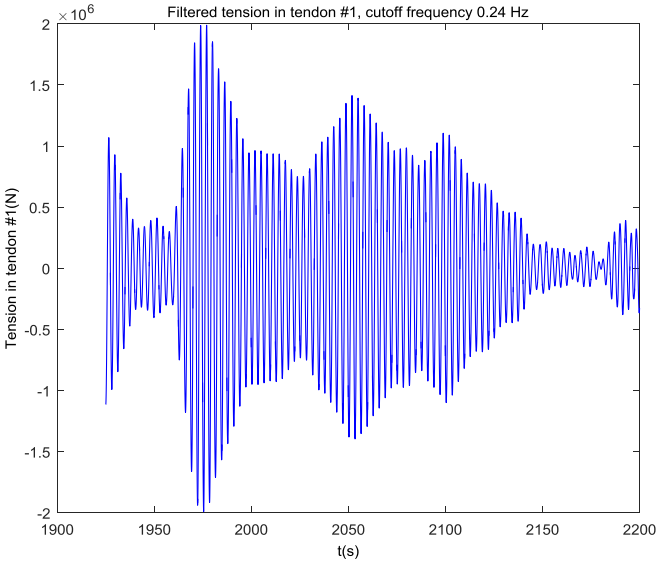

Fig. 9. High-frequency component of the tension in tendon #1.

According to this criterion, ringing is not observed within 3000 s of simulation time because all of the extreme values are less than four times the corresponding standard deviations, and none of the kurtosis values exceed 2.0.

Ringing is more likely to be excited by highly asymmetric waves. In this simulation, the irregular wave is generated based on the superposition of airy waves, which results in a nearly symmetric wave profile. Further investigations should be performed to confirm whether the consideration of nonlinear waves and higher-order potentials neglected in this paper may lead to ringing.

5.5. Effect of aerodynamic coupling

The effects of aerodynamic coupling on the pitch resonance are studied by running simulations with and without winds. Here, the steady-state wind velocity is 11 m/s, which is close to the rated wind speed of the 5 MW wind turbine, and the rotor angular velocity is fixed at the rated value of 12.1 rpm. The PSDs of the surge, pitch, and tensions in tendons #1 and #2 are plotted and shown in Fig. 10.

The surge PSDs exhibit small differences, which indicates that the hydrodynamic loads dominate the surge response, and the surge is slightly reduced by the damping effect of the winds. The pitch PSD is slightly increased at the wave frequency in the presence of winds because of the aerodynamic coupling effect from surge motion indicated by Eq. (4). Because the TLP is compliant

Table 8
Statistics of the high-frequency pitch and tensions in tendons #1 and #2.

	Pitch (deg)	Tension #1(N)	Tension #2(N)
Mean	2.753E-06	6.454E+03	6.358E+03
Std.	2.858E-02	6.456E+05	3.235E+05
Skewness	7.295E-04	1.212E-03	−1.129E-02
Kurtosis	1.091E+00	1.062E+00	1.091E+00
Maximum	1.080E-01	2.471E+06	1.235E+06
Minimum	−1.073E-01	−2.427E+06	−1.215E+06

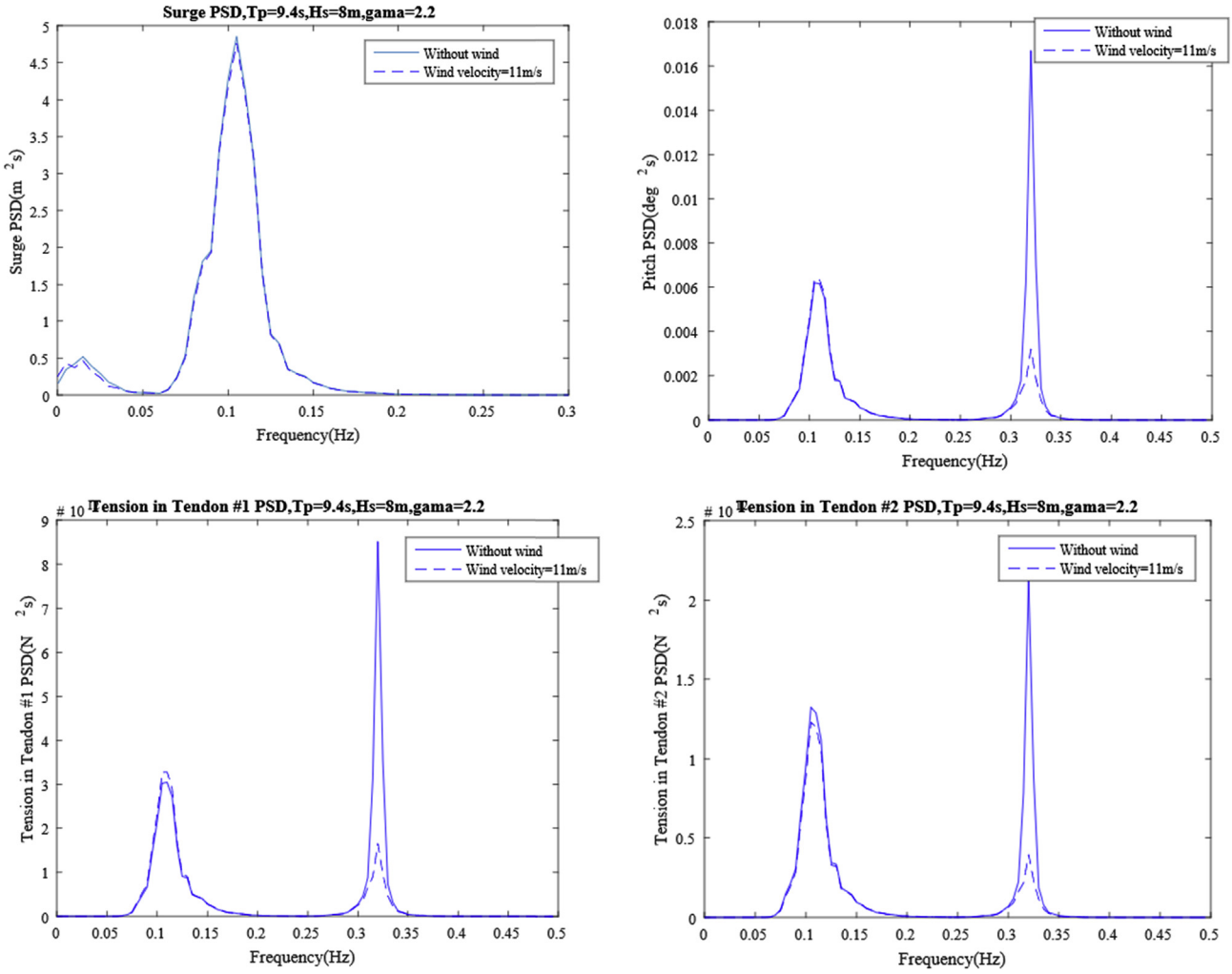

Fig. 10. Comparison of the dynamic responses of the surge, pitch and tendon tensions with and without steady-state winds.

Table 9
Statistics of motions and tendon tensions for a wind velocity of 11 m/s.

	Surge (m)	Heave (m)	Pitch (deg)	Tension #1 (N)	Tension #2 (N)
Mean	9.191E+00	−1.364E-01	8.566E-02	6.931E+06	4.036E+06
Std.	9.838E-01	5.362E-02	3.944E-02	8.892E+05	5.203E+05
Skewness	−1.226E-01	−2.090E-01	4.524E-02	3.077E-03	2.177E-02
Kurtosis	−5.148E-03	1.011E-01	1.568E-01	2.981E-01	3.267E-01
Maximum	1.264E+01	1.143E-02	2.342E-01	1.041E+07	6.150E+06
Minimum	5.978E+00	−3.620E-01	−5.970E-02	3.413E+06	2.071E+06

against horizontal loads and stiff against vertical loads, surge motion is much more appreciable than pitch motion. Therefore, although pitch motion causes an additional excitation force for surge motion through aerodynamic coupling, as suggested by Eq. (3), the excitation force is too small to be apparent. However, the additional aerodynamic excitation force for pitch motion caused by surge motion is sufficient to increase the pitch responses at the wave frequency, although at the pitch resonant frequency, aerodynamic damping significantly reduces the pitch resonant motion. The PSDs of the tension in tendon #1 show a similar trend with those of pitch motion. At the wave frequency, the PSD of the tension in tendon #2 is reduced in the presence of winds. This result is inconsistent to the behavior of pitch and tension in tendon #1, which is likely to be attributed to the effect of changed natural frequencies because of changed tension in tendon #2. The statistics in the presence of winds are listed in Table 9.

The standard deviations of the pitch and tendon tensions are reduced, which is anticipated based on their PSDs and caused by the damping effect of the aerodynamic forces, which significantly reduces the resonant motion. Both the maximum and minimum values of the tension in tendon #1 increase and those of tendon #2 decrease because the pitch moment induced by the rotor thrust force increases the mean value in tendon #1 and decreases the mean value in tendon #2. In addition, variations in the tensions are reduced because of aerodynamic damping, with the reduction caused by the combination of these two effects, indicating that aerodynamic forces mitigate the severity of extreme loads on tendons, which is beneficial for survivability. These forces also change

the dynamic response characteristics of the tendon system by changing the mean tensions, which leads to changes in the natural frequencies of the tendons' transversal motions. The natural transversal frequencies of a tensioned beam increase with increasing tension. Therefore, both the tension and natural transversal frequencies of tendon #1 increase because of the pitch moment induced by the rotor thrust, whereas those of tendon #2 decrease. This change causes different responses in tendons #1 and #2 to the excitations at different frequencies. The first structural natural period of the tendons is 3.69 s without an aerodynamic load. In the presence of steady-state winds, the natural period of tendon #1 decreases and nears the pitch resonant period, making it more sensitive to pitch resonance. As a result, the kurtosis of the tension in tendon #1 increases because of the pitch resonance, whereas the natural period of tendon #2 increases and becomes less sensitive to the pitch resonance, leading to a decrease in the kurtosis.

6. Conclusions

This work presents the coupled dynamic responses of the surge, pitch and tendon tensions of a TLP-type floating wind turbine predicted using a newly developed time-domain code, CRAFT. The capability of CRAFT has been verified by comparing its simulation results with those predicted using FAST as well as with experimental results.

The following conclusions regarding the pitch resonance induced by viscous drag forces can be drawn from the simulation results.

(1) The viscous forces on both the column and pontoons and those on the tendons contribute to higher harmonic excitation in the pitch resonance, with the former dominating the response. The excitation effect of the viscous force on the tendons decreases with increasing wave periods, and the damping effect increases and overwhelms the excitation effect.
(2) Higher harmonic pitch responses have much smaller amplitudes than those of the relatively lower harmonic responses, whereas both have a strong dependence on wave height. Regardless of the order, the amplitudes of all higher harmonic resonant pitch motions are proportional to the wave height to a power of one and half when the wave height is small. The amplitude of the third higher harmonic resonant pitch motion increases with increasing wave heights for small waves, reaching a maximum when the wave height attains a threshold and decreasing with further increases in the wave height. These responses are mainly caused by the increasing damping effect of the viscous drag force.
(3) The third harmonic excitation produces well-defined pitch resonance and tendon springing for a random sea state. These motions are found to be highly nonlinear, and their probability distributions deviate from that of a Gaussian distribution. The probability of experiencing extreme loads is also significantly increased because of springing.
(4) Aerodynamic loads provide significant damping for pitch motion, which mitigates the severity of resonant motion and also changes the dynamic response characteristics of the tendons by changing their mean tensions. This is consistent with the experimental findings in Koo et al. [5]. An additional coupling between surge and pitch is observed, and it is caused by the presence of aerodynamic forces. This effect slightly increases the pitch response at the wave frequency.

Acknowledgements

The authors would like to acknowledge the State Key Lab of Ocean Engineering in Shanghai Jiao Tong University. The financial support from the Natural Science Fund of China (Grant No. 51239007) is also gratefully acknowledged by the authors.

References

[1] M. Karimirad, M. Torgeir, Effect of aerodynamic and hydrodynamic damping on dynamic response of a spar type floating wind turbine, Development 2 (2010) 3.
[2] G. Fulton, et al., Semi-submersible Platform and Anchor Foundation Systems for Wind Turbine Support, Tech. rep.NREL/SR-500–40282, National Renewable Energy Laboratory, 2007.
[3] P. Sclavounos, et al., Floating offshore wind turbines: tension leg platform and taught leg buoy concepts supporting 3–5 MW wind turbines, in: European Wind Energy Conference EWEC 2010, Warsaw, Poland, 2010.
[4] D. Matha, Model Development and Loads Analysis of an Offshore Wind Turbine on a Tension Leg Platform with a Comparison to Other Floating Turbine Concepts: April 2009, No. NREL/SR-500–45891, National Renewable Energy Laboratory (NREL), Golden, CO, 2010.
[5] B.J. Koo, et al., Model tests for a floating wind turbine on three different floaters, J. Offshore Mech. Arct. Eng. 136 (2) (2014) 020907.
[6] O. Faltinsen, Sea Loads on Ships and Offshore Structures, vol. 1, Cambridge University Press, 1993.
[7] M.C. Shen, Z.Q. Hu, T. Gen, Coupled hydrodynamic and aerodynamic response analysis of a tension-leg platform floating wind turbine, J. Ship Mech. (2016) (accepted for publication in 2016).
[8] G.M. Stewart, et al., Calibration and validation of a FAST floating wind turbine model of the DeepCwind scaled tension-leg platform, in: 22nd International Offshore and Polar Engineering Conference, Rhodes, Greece, June, 2012.
[9] W. Tao, Z. Jun, Hydrodynamics in deepwater TLP tendon design, J. Hydrodyn. Ser. B 18 (3) (2006) 386–393.
[10] J.R. Paulling, W.C. Webster, A Consistent, large-amplitude analysis of the coupled response of a TLP and Tendon system, in: Proceedings Fifth International Mechanics and Arctic Engineering Symposium, vol. III, 1986, pp. 126–133.
[11] S. Ahmad, Stochastic TLP response under long crested random sea, Comput. Struct. 61 (6) (1996) 975–993.
[12] M.M. Gadagi, H. Benaroya, Dynamic response of an axially loaded tendon of a tension leg platform, J. Sound Vib. 293 (1) (2006) 38–58.
[13] L. Roald, et al., The effect of second-order hydrodynamics on floating offshore wind turbines, Energy Procedia 35 (2013) 253–264.
[14] X.H. Chen, et al., Coupled dynamic analysis of a mini TLP: comparison with measurements, Ocean. Eng. 33 (1) (2006) 93–117.
[15] P.J. Moriarty, A.C. Hansen, AeroDyn Theory Manual, National Renewable Energy Laboratory, Golden, Colorado, USA, 2005.
[16] T. Burton, et al., Wind Energy Handbook, John Wiley & Sons, 2001.
[17] C.C. Mei, M. Stiassnie, D.K.P. Yue, Theory and Applications of Ocean Surface Waves: Linear Aspects, vol. 23, World Scientific, 2005, p. 449.
[18] C.H. Lee, WAMIT Theory Manual, Massachusetts Institute of Technology, Department of Ocean Engineering, 1995.
[19] P.W. Bearman, P.R. Mackwood, Measurements of the hydrodynamic damping force of circular cylinders, in: Behaviour of Offshore Structural Conference, BOSS 92, vol. II, BPP Technical Services LTD, London, 1992, p. 405.
[20] P.W. Bearman, et al., Forces on cylinders in viscous oscillatory flow at low Keulegan-Carpenter numbers, J. Fluid Mech. 154 (1985) 337–356.
[21] J.R. Hoff, Estimation of Linear and Quadratic Roll Damping from Free-decay Tests, 2001. Tech. Rep. 601882, NTNU.
[22] J.M. Jonkman, Definition of the Floating System for Phase IV of OC3, National Renewable Energy Laboratory, Golden, CO, USA, 2010.
[23] H.P. Williazm, et al., Numerical Recipes, Cambridge Press, 2000, pp. 1083–1097.
[24] K.B. Davies, S.J. Leverett, M.W. Spillane, Ringing response of TLP and GBS platforms, in: Proc 7th Int Conf Behavior Offshore Structures, vol. 2, 1994, pp. 569–585.
[25] E.R. Jefferys, R.C. Rainey, Slender body models of TLP and GBS 'Ringing', in: Proc Int Conf Behavior Offshore Structures, vol. 2, 1994, pp. 587–605.